




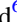











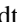
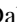










CrossMark

# Space Telescope and Optical Reverberation Mapping Project. XI. Disk-wind Characteristics and Contributions to the Very Broad Emission Lines of NGC 5548

M. Dehghanian<sup>1</sup> , G. J. Ferland<sup>1</sup> , G. A. Kriss<sup>2</sup> , B. M. Peterson<sup>2,3,4</sup> , K. T. Korista<sup>5</sup> , M. R. Goad<sup>6</sup> , M. Chatzikos<sup>1</sup> , F. Guzmán<sup>1</sup> , G. De Rosa<sup>2</sup> , M. Mehdipour<sup>7</sup> , J. Kaastra<sup>7,8</sup> , S. Mathur<sup>3,4</sup> , M. Vestergaard<sup>9,10</sup> , D. Proga<sup>11</sup> , T. Waters<sup>11</sup> , M. C. Bentz<sup>12</sup> , S. Bisogni<sup>13</sup> , W. N. Brandt<sup>14,15,16</sup> , E. Dalla Bontà<sup>17,18</sup> , M. M. Fausnaugh<sup>19</sup> , J. M. Gelbord<sup>20</sup> ,

Keith Horne<sup>21</sup> , I. M. McHardy<sup>22</sup> , R. W. Pogge<sup>3,4</sup> , and D. A. Starkey<sup>21</sup> 

<sup>1</sup> Department of Physics and Astronomy, The University of Kentucky, Lexington, KY 40506, USA

<sup>2</sup> Space Telescope Science Institute, 3700 San Martin Drive, Baltimore, MD 21218, USA

<sup>3</sup> Department of Astronomy, The Ohio State University, 140 W 18th Avenue, Columbus, OH 43210, USA

<sup>4</sup> Center for Cosmology and AstroParticle Physics, The Ohio State University, 191 West Woodruff Avenue, Columbus, OH 43210, USA

<sup>5</sup> Department of Physics, Western Michigan University, 1120 Everett Tower, Kalamazoo, MI 49008-5252, USA

<sup>6</sup> Department of Physics and Astronomy, University of Leicester, University Road, Leicester, LE1 7RH, UK

<sup>7</sup> SRON Netherlands Institute for Space Research, Sorbonnelaan 2, 3584, CA Utrecht, The Netherlands

<sup>8</sup> Leiden Observatory, Leiden University, PO Box 9513, 2300 RA Leiden, The Netherlands

<sup>9</sup> DARK, Niels Bohr Institute, University of Copenhagen, Vibenshuset, Lyngbyvej 2, DK-2100 Copenhagen Ø, Denmark

<sup>10</sup> Steward Observatory, University of Arizona, 933 North Cherry Avenue, Tucson, AZ 85721, USA

<sup>11</sup> Department of Physics & Astronomy, University of Nevada, Las Vegas, 4505 S. Maryland Pkwy, Las Vegas, NV 89154-4002, USA

<sup>12</sup> Department of Physics and Astronomy, Georgia State University, 25 Park Place, Suite 605, Atlanta, GA 30303, USA

<sup>13</sup> INAF—Istituto di Astrofisica Spaziale e Fisica Cosmica Milano, via Corti 12, I-20133 Milano, Italy

<sup>14</sup> Department of Astronomy and Astrophysics, Eberly College of Science, The Pennsylvania State University, 525 Davey Laboratory, University Park, PA 16802, USA

<sup>15</sup> Department of Physics, The Pennsylvania State University, 104 Davey Laboratory, University Park, PA 16802, USA

<sup>16</sup> Institute for Gravitation and the Cosmos, The Pennsylvania State University, University Park, PA 16802, USA

<sup>17</sup> Dipartimento di Fisica e Astronomia “G. Galilei,” Università di Padova, Vicolo dell’Osservatorio 3, I-35122 Padova, Italy

<sup>18</sup> INAF-Osservatorio Astronomico di Padova, Vicolo dell’Osservatorio 5 I-35122, Padova, Italy

<sup>19</sup> Department of Physics, and Kavli Institute for Astrophysics and Space Research, Massachusetts Institute of Technology, Cambridge, MA 02139, USA

<sup>20</sup> Spectral Sciences Inc., 4 Fourth Avenue, Burlington, MA 01803, USA

<sup>21</sup> SUPA Physics and Astronomy, University of St. Andrews, Fife, KY16 9SS Scotland, UK

<sup>22</sup> School of Physics and Astronomy, University of Southampton, Highfield, Southampton, SO17 1BJ, UK

Received 2020 May 1; revised 2020 June 9; accepted 2020 June 11; published 2020 August 3

## Abstract

In 2014 the NGC 5548 Space Telescope and Optical Reverberation Mapping campaign discovered a two-month anomaly when variations in the absorption and emission lines decorrelated from continuum variations. During this time the soft X-ray part of the intrinsic spectrum had been strongly absorbed by a line-of-sight (LOS) obscurer, which was interpreted as the upper part of a disk wind. Our first paper showed that changes in the LOS obscurer produces the decorrelation between the absorption lines and the continuum. A second study showed that the base of the wind shields the broad emission-line region (BLR), leading to the emission-line decorrelation. In that study, we proposed the wind is normally transparent with no effect on the spectrum. Changes in the wind properties alter its shielding and affect the spectral energy distribution (SED) striking the BLR, producing the observed decorrelations. In this work we investigate the impact of a translucent wind on the emission lines. We simulate the obscuration using XMM-Newton, NuSTAR, and Hubble Space Telescope observations to determine the physical characteristics of the wind. We find that a translucent wind can contribute a part of the He II and Fe K $\alpha$  emission. It has a modest optical depth to electron scattering, which explains the fainter far-side emission in the observed velocity-delay maps. The wind produces the very broad base seen in the UV emission lines and may also be present in the Fe K $\alpha$  line. Our results highlight the importance of accounting for the effects of such winds in the analysis of the physics of the central engine.

*Unified Astronomy Thesaurus concepts:* Seyfert galaxies (1447); Active galaxies (17); Active galactic nuclei (16)

## 1. Introduction

The broad emission-line region (BLR) is closely associated with the central regions and the supermassive black hole (SMBH) in active galactic nuclei (AGNs). Reverberation mapping (RM; Blandford & McKee 1982; Peterson 1993) can determine the geometry and kinematics of the BLR, which can be used to infer the mass of the BH (Horne et al. 2004).

RM uses the time delay between the continuum and emission-line variations to determine the responsivity-weighted distance to the line-emitting region (Peterson et al. 2004), which is commonly taken to represent a characteristic size scale of the BLR. The time delay is, in fact, the travel time of the ionizing photons from the inner accretion disk region to the BLR gas. The duration of the delay depends on the causal connection between the broad emission-line gas and the ionizing continuum emission. This causal connection is one of the fundamental principles of RM.

In 2014, the most intensive RM campaign, AGN Space Telescope and Optical Reverberation Mapping (STORM;

De Rosa et al. 2015; Edelson et al. 2015; Fausnaugh et al. 2016; Goad et al. 2016; Mathur et al. 2017; Pei et al. 2017; Starkey et al. 2017; Dehghanian et al. 2019a; Kriss et al. 2019), observed the AGN NGC 5548 for six months. This unique data set has revealed several unexpected results. For a period of  $\sim 2$  months mid-way through the campaign, the continuum and broad emission-line variations were observed to decorrelate (Goad et al. 2016), the so-called “emission-line holiday.” At almost the same time, the continuum and narrow absorption lines also decorrelated (Kriss et al. 2019), the “absorption-line holiday.” These spectral holidays, along with the presence of an X-ray obscurer in our line of sight (LOS) to the SMBH (Kaastra et al. 2014), distinguish the 2014 version of NGC 5548 from normal AGNs. There is no part of the standard AGN scenario that produces holidays, so clearly something fundamental is missing (Dehghanian et al. 2019a, 2019b, hereafter D19a and D19b). This is an opportunity to determine the physics controlling the spectral holiday, to study AGN feedback, and develop scenarios about this central activity that affects the evolution of galaxies.

D19a show that the variation of the LOS obscurer covering factor (CF) produces the observed absorption-line holiday. Swift observations (Mehdipour et al. 2016) show that the absorption-line variations correlate with the CF (Figure 12 of D19a), so are consistent with this interpretation. D19b propose that the LOS obscurer is the upper part of a symmetric cylindrical disk wind that originates from the inner parts of the accretion disk and is interior to the BLR. As argued by D19b, the base of the wind forms an equatorial obscurer, filtering the spectral energy distribution (SED) before the ionizing photons strike the BLR, leading to the observed emission-line holiday.

In this work, we create potential models for the equatorial obscurer. Unlike the LOS obscurer, which can be studied by its absorption of the SED, the geometry and characteristics of the base of the wind are unknown. It does not absorb along our LOS, however, it filters the SED of the photons that reach the BLR. In the following Section we use STORM BLR observations to infer the properties of the obscurer. We use these constraints to narrow down the parameters and we propose a final model that not only reproduces the emission-line holiday (D19b), but is also consistent with the observations, while reproducing the absorption-line holiday (D19a).

Our preferred model of the base of the wind is also a major contributor to the observed broad iron  $K\alpha$  line. Both disk winds and broad Fe  $K\alpha$  emission are considered to be common properties of AGNs, and we propose that the SED filtering through the wind is too.

## 2. Physical Models of the Equatorial Obscurer

In this paper we consider new models of the equatorial obscurer. We do not provide new models of the BLR but rather rely on the results of D19b. Figure 4 of D19b shows that the equatorial obscurer will lead to a holiday if hydrogen is fully ionized and a  $\text{He}^+$  ionization front is present within it (their Case 2). All models in this paper have a column density adjusted so that the optical depth is 8 at 4 Rydberg. This optical depth belongs to the left threshold of Case 2 in D19b, and ensures the presence of the emission-line holiday.

We adopt the SED of Mehdipour et al. (2015) in CLOUDY (developer version, Ferland et al. 2017) and an open geometry<sup>23</sup> for the equatorial obscurer. An open geometry is appropriate

when the emission-line cloud CF is small since diffuse emission is assumed to escape from the AGN. The global BLR CF is about 50% (integrated cloud covering fraction; Korista & Goad 2000) and the equatorial obscurer must cover at least this much. So, it is intermediate between an open and closed geometry. Inspired by Figure 1 of D19b, we adopt an open geometry. In order to make our predictions more accurate, we increased the number of levels to  $n = 100$  for H like atoms. This allows a better representation of the collision physics that occurs within higher levels of the atom. We also set the spectral resolution to  $5000 \text{ km s}^{-1}$ . Changing the velocity width does not resolve the lines but changes the line-to-continuum contrast ratio to simulate a spectrometer measuring an unresolved line. We further assume photospheric solar abundances (Ferland et al. 2017).

With the assumptions above, we computed two-dimensional grids of photoionization models, similar to those of Korista et al. (1997). Each grid consists of a range of total hydrogen density,  $10^{10} \text{ cm}^{-3} < n(\text{H}) < 10^{18} \text{ cm}^{-3}$ , and a range of incident ionizing photon flux,  $10^{20} \text{ s}^{-1} \text{ cm}^{-2} < \phi(\text{H}) < 10^{24} \text{ s}^{-1} \text{ cm}^{-2}$ . The right vertical axis on all plots (Figures 1–3) shows the distance from the incident ionizing continuum source in light days. The flux of ionizing photons  $\phi(\text{H})$ , the total ionizing photon luminosity  $Q(\text{H})$ , and the distance in light days are related by

$$\phi(\text{H}) = \frac{Q(\text{H})}{4\pi r^2}. \quad (1)$$

For the SED of Mehdipour et al. (2015) and the observed luminosity of  $L$  (1–1000 Ryd) =  $2 \times 10^{44} \text{ erg s}^{-1}$ , the  $Q(\text{H}) = 1.81 \times 10^{54} \text{ s}^{-1}$ .

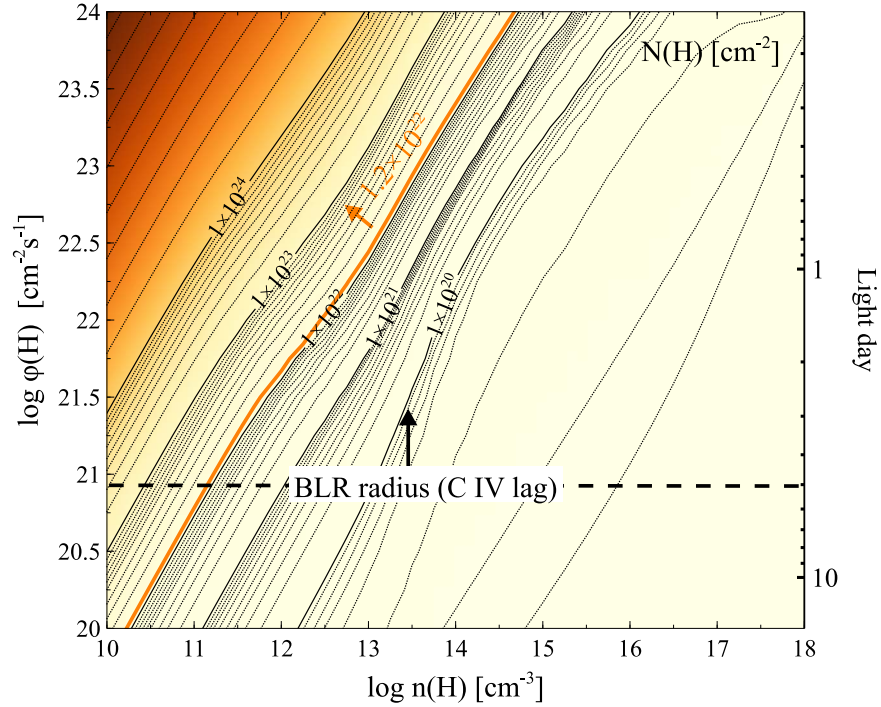
The STORM campaign reports observed lags between 2 and 9 light days for various strong emission lines (De Rosa et al. 2015, Table 4). In Figure 1, we show contours of the predicted obscurers column density. As mentioned earlier, we maintain a constant optical depth of 8 at an energy of 4 Rydbergs, the lower limit to have a holiday (D19b, Figure 4).

Next, we combine these predictions with the observations to derive the properties of the equatorial obscurer.

Before going on, we establish a nomenclature for the different components that we discuss in this paper. For the case of UV lines, Goad et al. (2016) and many other previous works report the total “time-averaged broad emission line (BEL) equivalent widths (EWs)” We refer to this as the “total” emission. Subsequent work by Kriss et al. (2019) models this total emission as the combination of three components: a “broad” component, a “medium broad” component, and a “very broad” component. The sum of the two first components (broad and medium broad) dominates in the line core, and we refer to them as the BLR/core. For C IV line, these components have FWHMs of  $3366 \pm 15$  and  $8345 \pm 20 \text{ km s}^{-1}$ , with an average of  $\sim 5000 \text{ km s}^{-1}$ . Our calculations in Section 3 suggest that the very broad component (FWHM =  $16367 \pm 18 \text{ km s}^{-1}$ ; Kriss et al. 2019) forms in the equatorial obscurer. For reference, Table 1 of Kriss et al. (2019) reports that the very broad component of C IV comprises almost 47% of the total emission.

For Fe  $K\alpha$ , Cappi et al. (2016) report the presence of a time-steady “narrow” component with an upper-limit of  $2340 \text{ km s}^{-1}$  on the line width, or to be specific,  $\text{FWHM} \leq 5500 \text{ km s}^{-1}$ . This is very similar to the BLR component of C IV (broad plus medium broad; Kriss et al. 2019). Assuming the line is broadened by orbital motions, and adopting the BH mass quoted by Cappi et al. (2016),

<sup>23</sup> Refer to Section 2.3.4 of the CLOUDYs documentation (Ferland et al. 2017).



**Figure 1.** Contours show total hydrogen column density of the equatorial obscurer as a function of the flux of ionizing photons and the hydrogen density. The orange line indicates the LOS obscurer column density (D19a) and the dashed black line shows the location of the BLR based on the observed C IV lag.

they argue that this component forms a few light days away from the central source (0.006 pc), consistent with the lag observed for C IV. We refer to this component as the “BLR” Fe K $\alpha$  emission. The signal-to-noise (S/N) ratios of the X-ray spectra do not permit a definitive detection of the very broad component modeled in the Hubble Space Telescope (HST) data, although Cappi et al. (2016) note that there appears to be a broad, redshifted component underlying the Fe K $\alpha$  profile.

### 3. Wind Properties from the Observations

The equatorial obscurer has a higher column density than the LOS obscurer since it is closer to the accretion disk, the site where the wind is launched. The orange line in Figure 1 shows the column density of the LOS obscurer,  $N(\text{H}) = 1.2 \times 10^{22} \text{ cm}^{-2}$  (Kaastra et al. 2014). The orange arrow shows the direction of possible higher column density obscurers.

The horizontal dashed black line indicates the location of the BLR adopting the C IV lag reported by De Rosa et al. (2015). To ensure that the base of the wind is located between the central SMBH and the BLR, we must choose an obscurer with a smaller distance (higher flux of ionizing photons) from the continuum source, than that for the BLR, the region suggested by the black arrow.

As Figure 1 shows, lines with constant column density are almost parallel for  $N(\text{H}) > 10^{21} \text{ cm}^{-2}$ , and their values increase toward the upper-left corner, closer to the source. These lines also represent a nearly constant ionization parameter, which increases toward the upper-left corner.

The properties of the equatorial obscurer are constrained by observations. The equatorial obscurer is a source of emission itself since energy is conserved, and it must re-radiate the energy that is absorbed. If the equatorial obscurer emission is strong enough, then it produces a second emission-line region between the original BLR and the source. Since re-emission by

the obscurer is not evident in the observations, we must find a model of the obscurer, which not only explains the holiday, but also does not dominate the strong lines seen by HST and XMM-Newton. To do this, we considered the total observed equivalent widths (EWs) of strong emission lines from the STORM data (Goad et al. 2016; Pei et al. 2017) and the total luminosity of Fe K $\alpha$  observed by XMM-Newton (Mehdipour et al. 2015).

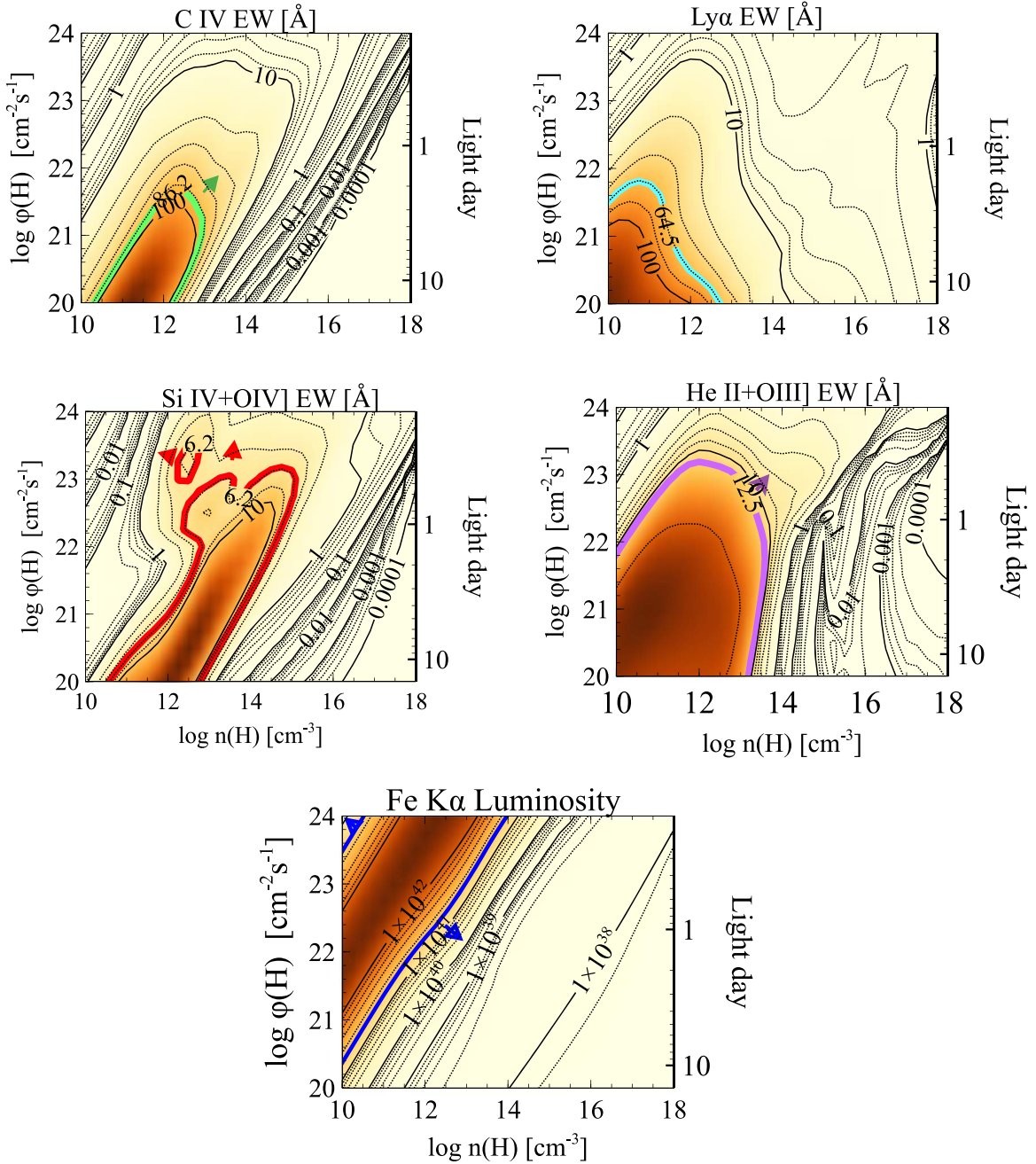
In general, an obscuring cloud may cover only a small fraction of the continuum source, as in the leaky LOS obscurer shown in Figure 6 of D19a, or it can fully cover the continuum source (CF = 100% in their figure). Here we assume that the equatorial obscurer fully covers the central object along the LOS of the BLR, which is the preferred situation explained by D19b.

We wish to directly compare our predictions with the observations. We report all lines as EW relative to the continuum at 1215 Å so that ratios of EWs are the same as ratios of intensities.

The EW is proportional to the ratio of a line luminosity to the continuum. We assume that the continuum is isotropic and that HST had an unextinguished view of it. The continuum luminosity is not affected by the equatorial obscurer’s CF. The luminosities of lines emitted by the equatorial obscurer are linearly proportional to the equatorial global CF, the fraction of  $4\pi$  steradian covered by the obscurer. The equatorial obscurer CF is not known but must be at least 50% if it is to shield the BLR. We report EWs for full coverage with the understanding that the actual EW of the obscurer is

$$\text{EW}(\text{obscurer}) = \frac{\Omega}{4\pi} \times \text{EW}(\text{pred}) \sim 50\% \text{EW}(\text{pred}). \quad (2)$$

On the other hand, the equatorial obscurer is not a dominant contributor to the emission lines. As a first step in the modeling, we set a limit so that the amount of emission from



**Figure 2.** Upper four panels show the predicted EW of strong lines emitted by the equatorial obscurer as the contours. The colored lines indicate the HST observed value and arrows show the direction in which the equatorial obscurer must be chosen in order for its emission to not dominate the HST emission lines. All the EWs are relative to the 1215 Å continuum. The lowest panel shows the predicted luminosity of Fe Kα as the contours and the blue lines show the XMM-Newton observed values.

the obscurer is less than half of the total emission. To choose this value, we were motivated by the ratio of the flux of very broad C IV to the flux of total observed C IV, 47%, as measured by Kriss et al. (2019):

$$\text{EW}(\text{obscurer}) \leq 50\% \text{EW}(\text{observed}). \quad (3)$$

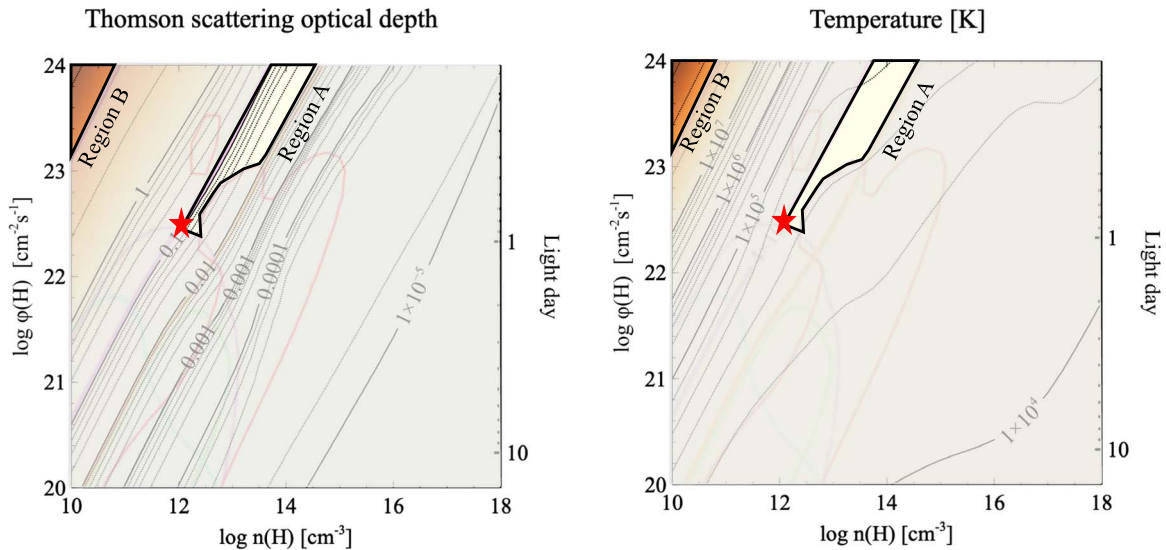
Based on Equations (2) and (3), the two factors of 50% cancel

$$\text{EW}(\text{pred}) \leq \text{EW}(\text{observed}), \quad (4)$$

which means any model of the equatorial obscurer that produces lines with EW less than the observed total values are allowed. We map the obscurer's predicted emission lines in

Figure 2. We also include the observed values as colored lines in each panel. The arrows show the physical conditions where the obscurer will *not* dominate the emission-line fluxes of observed HST spectrum.

The lowest panel of Figure 2 shows the predicted luminosity of Fe Kα for full coverage. When the obscurer is highly ionized, Fe Kα is strong (dark orange). It becomes weaker in the extreme upper-left corner where the obscurer is fully ionized. In this regime, there are few bound electrons and there is no iron emission line or edge. The observed time-averaged value of its luminosity for the 2013 campaign is  $(2.0 \pm 0.3) \times 10^{41} \text{ erg s}^{-1}$  (Mehdipour et al. 2015) and is indicated by the blue lines in Figure 2.



**Figure 3.** Left panel maps the Thomson scattering optical depth and the right panel maps the temperature of the obscurer. A and B are two regions with allowed properties of the equatorial obscurer. The red star indicates our preferred model, which is the most consistent with all observational constraints.

Satisfying the constraints from Equations (2) and (3) guarantees that the obscurer does not produce strong emission lines. For the rest of the modeling, we assume this holds for all lines except He II and broad Fe  $K\alpha$ . As discussed below, the lag profiles measured by Horne et al. (2020) show that He II forms very close to the central source. We assume that all of the UV He II comes from the obscurer. The Fe  $K\alpha$  profile discussed below is consistent with half of the line forming in the BLR with a broad base forming in the obscurer.

Figure 3 shows the regions which satisfy all the constraints inferred from Figures 1 and 2. All the forbidden areas are colored in gray. The right panel shows the variation of the temperature as a function of both the flux and the density. The temperature increases as the distance to the central source decreases. The left panel maps the Thomson scattering optical depth as a function of flux and density. Gas in the upper-left corner of the plot has a significant column density and Thomson scattering optical depth. Note that the soft X-ray observations constrain the ionization parameter but not the density or distance from the center so any location along the line is allowed. In both panels, all the constraints from Figure 2 are shown as faint colored lines, in order to show how we recognize the forbidden region.

As shown in both panels, there are two possible regions for the obscurer’s properties:

**Region A:**  $r < 1$  light days,  $10^{12} \text{ cm}^{-3} < n(\text{H}) < 10^{14} \text{ cm}^{-3}$ ,  $\phi(\text{H}) > 10^{22.4} \text{ s}^{-1} \text{ cm}^{-2}$ ,  $10^{4.6} \text{ K} < T < 10^{4.8} \text{ K}$ , and  $1.2 \times 10^{22} \text{ cm}^{-2} \leq N(\text{H}) < 2 \times 10^{23} \text{ cm}^{-2}$ . The low-density bound of the region is set by the luminosity of Fe  $K\alpha$ , the lower bound by He II, and the high-density bound by LOS column density. It has a Thomson scattering optical depth between 0.01 and 0.1.

**Region B:**  $r < 0.4$  light days, with  $n(\text{H}) < 10^{11} \text{ cm}^{-3}$ , and  $\phi(\text{H}) > 10^{23} \text{ s}^{-1} \text{ cm}^{-2}$ ,  $T \geq 3 \times 10^7$ , and  $N(\text{H}) \geq 10^{24} \text{ cm}^{-2}$ . It has a very high ionization parameter and is Compton thick (Figure 2). The lower limit to this region is set by the Fe  $K\alpha$  emission. The Thomson scattering optical depth is  $\tau_e \geq 4$ .

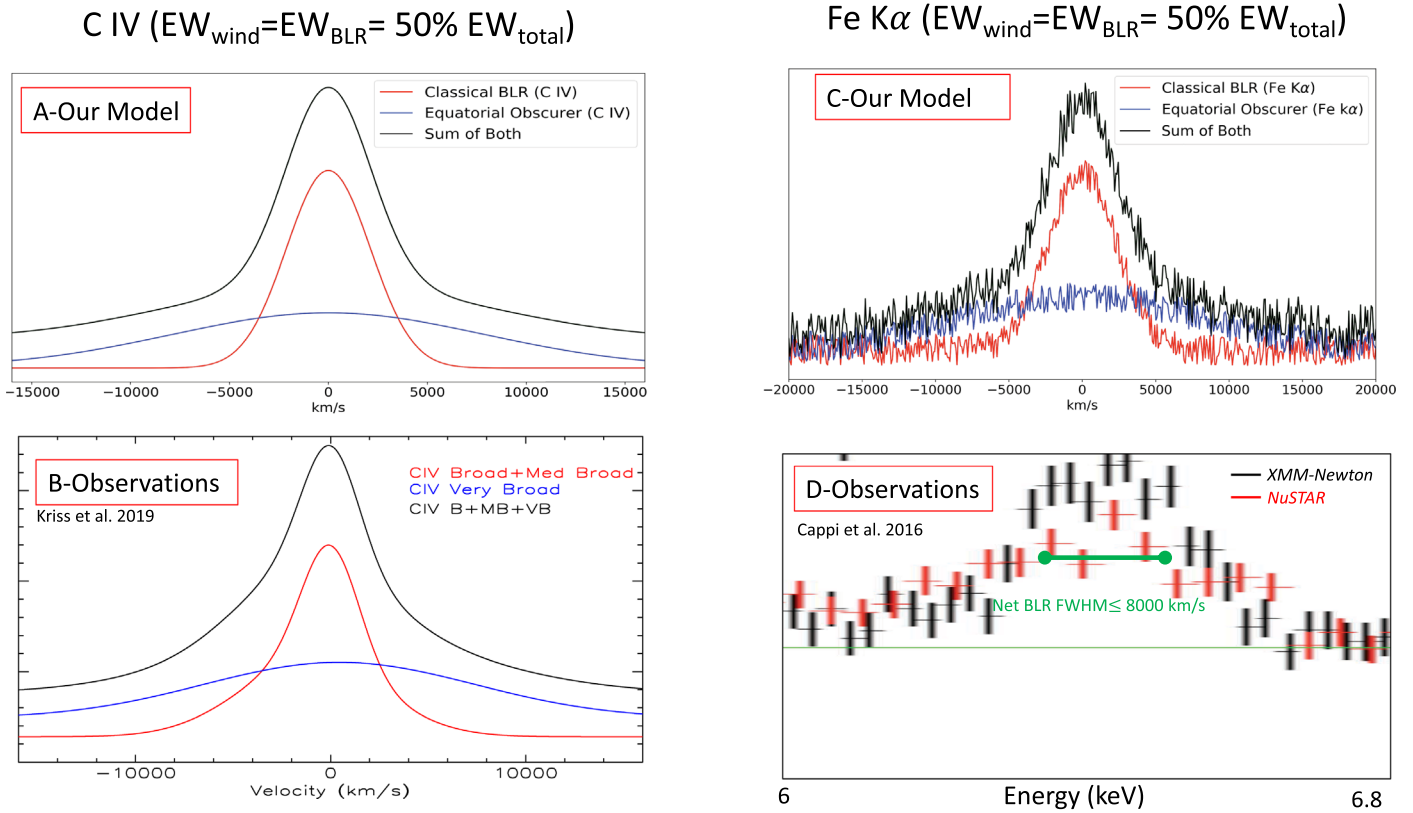
We prefer region A since it produces significant very broad He II and Fe  $K\alpha$  emission, but produces other UV lines with EWs less than half the observed values. The He II velocity-delay map sets a  $\leq 5$  day limit to the lag (Horne et al. 2020).

This is consistent with almost all of the observed He II being produced in the equatorial obscurer. As with the UV lines, we assume that half of the Fe  $K\alpha$  forms in the obscurer, with the other half in the BLR. Below we show that this is also suggested by the Fe  $K\alpha$  line profile, in which half of the line EW forms in the BLR and the rest is a strong broad component that forms in the equatorial obscurer. This might be the very broad Fe  $K\alpha$  component mentioned by Cappi et al. (2016) and is produced in the obscurer.

Region B is not of interest for our model of the wind since the EWs of the broad UV lines produced by any winds chosen from this region are almost 1% of the total observed values. Moreover, a wind chosen from region B will be very close to the central source and will emit lines much broader than what was observed.

The parameters for our final preferred model,  $\phi(\text{H}) \approx 10^{22.5} \text{ s}^{-1} \text{ cm}^{-2}$ ,  $n(\text{H}) \approx 10^{12} \text{ cm}^{-3}$ ,  $T \approx 5 \times 10^4 \text{ K}$ , and  $\tau_e \approx 0.1$  are shown with a star in Figure 3. A wind with these parameters is our favorite model in region A, since it has a major contribution to the He II and Fe  $K\alpha$  emissions. Any other wind selected from region A will emit lower values of the mentioned lines. These conditions place the wind/equatorial obscurer at about one light day from the central source. Please note that although the mentioned hydrogen density seems to correspond to the changing look portion of Figure 4 of D19b, since the current paper has adopted a different  $\phi(\text{H})$  for the equatorial obscurer, the ionization parameter is nearly the same as case 2 in D19b. This means an obscurer with mentioned  $\phi(\text{H})$  and  $n(\text{H})$  belongs to the case 2 discussed in D19b and reproduces the holiday. This was expected since by keeping the optical depth constant, we made sure that all of the models in this paper belong to case 2 of D19b.

Figure 4 compares our predictions for the C IV and Fe  $K\alpha$  line profiles with the observations. To illustrate our preferred model (panels A and C), we adopt a SMBH mass of  $M = (5.2 \pm 0.2) \times 10^7 M_\odot$  (Bentz & Katz 2015). Assuming Keplerian motion and the equations given in the first paragraph in Section 5.1 of Cappi et al. (2016), the lines produced by the equatorial obscurer have a FWHM of  $18,500 \pm 3500 \text{ km s}^{-1}$ . The more recent BH mass estimations are about 50% larger than our adopted value



**Figure 4.** This figure compares our model with the observations from HST, XMM-Newton, and NuSTAR. Panels A and B show the case for C IV, for which the obscurer produces a very broad component (panel A, blue) with an EW of half of that produced by the BLR (panel A, red). Panels C and D show the case for Fe K $\alpha$ , for which the obscurer produces a very broad component (panel C, blue) with an EW equal to that produced by the BLR (panel C, red). It is plausible that a broad base similar to C IV is present, although the S/N is not high enough to say for sure. In both cases our predictions are very similar to the observations, suggesting that the disk wind could be responsible for the observed very broad emission-line components.

(Home et al. 2020). This represents the uncertainty in the BH mass measurements and causes 20% uncertainty on the FWHM of our model, since the line width estimation depends on the BH mass. We adopt the mass determined by Bentz & Katz (2015), to be consistent with Kriss et al. (2019).

Figure 4’s panels A (theory) and B (HST observations) show the case for C IV, in which we are using arbitrary vertical offsets in flux, simply for illustrative purposes. To produce panel A, we assume that the equatorial obscurer is emitting C IV with an EW half of the observed value and with  $\text{FWHM} = 18,500 \text{ km s}^{-1}$  (blue line), while the BLR emits the flux with  $\text{FWHM} = 5000 \text{ km s}^{-1}$  (red line; Kriss et al. 2019). Panel B is the best-fit model to the HST STORM observations (Kriss et al. 2019). Those panels suggest that the equatorial obscurer could well be responsible for the very broad component.

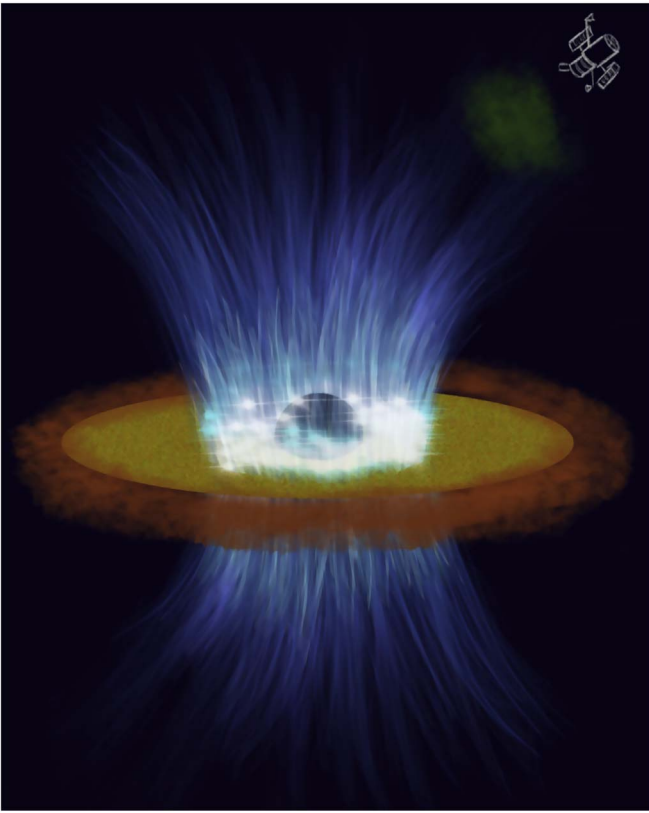
Figure 4’s panels C (theory) and D (NuSTAR and XMM-Newton observations, 2013 July 11–12, July 23–24, and December 20–21) show the same thing for the Fe K $\alpha$  line, but this time we assume that the obscurer produces the emission line with an EW equal to that observed and a  $\text{FWHM} = 18,500 \pm 3500 \text{ km s}^{-1}$  (blue line), while the BLR emits Fe K $\alpha$  with  $\text{FWHM} = 5500 \text{ km s}^{-1}$  (red line; Cappi et al. 2016). Panel D shows the observations of Cappi et al. (2016) in which the vertical axis indicates the data as the ratio to a single power-law continuum model fitted to the XMM-Newton (black) and NuSTAR (red) observations. The green horizontal line shows the net FWHM which is calculated by adding the widths of two

Gaussian functions with the same central wavelength position in quadrature (the core corresponding to the observed broad Fe K $\alpha$   $\text{FWHM} = 5500 \text{ km s}^{-1}$  and the XMM-Newton resolution with  $dE/E = 1/50$ , so  $\text{FWHM} = 6000 \text{ km s}^{-1}$ ). This results in a net BLR  $\text{FWHM} \leq 8000 \text{ km s}^{-1}$ , consistent with the BLR core observed by HST and suggests that the core of the observed Fe K $\alpha$  profile is in good agreement with our model. Comparing panels C and D, which are equally scaled, shows that the very broad emission from the obscurer might easily hide under the total emission and be just seen as a very broad continuum. This very broad base may be observable in Panel D at  $\pm 7000 \text{ km s}^{-1}$ .

The total observed Fe K $\alpha$  profile (panel C) is similar to the C IV seen by STORM, although this is not a strong statement due to the S/N ratio in the X-ray data. Indeed, the total C IV is consistent with the “narrow” Fe K $\alpha$  discussed in Cappi et al. (2016). Motivated by this similarity, we propose that this line also includes the classical BLR emission and a very broad component originated from the wind, hidden in the noise. This scenario is a testable hypothesis for our model and can be the subject of future observations with Chandra/High-Energy Transmission Grating (HETG).

#### 4. Discussion and Summary

Here, we have used HST and XMM-Newton observational constraints to derive a model of the equatorial obscurer. We have shown that the equatorial obscurer, which modifies the SED to produce the emission-line holiday, is itself a significant source of line emission, solving several long-standing problems



**Figure 5.** Cartoon of the disk wind in NGC 5548 (not to scale). The disk wind (blue) surrounds the central black hole and extends to the LOS to HST in the upper-right corner. The BLR is shown as the orange cloud around the disk. The green cloud at the upper right shows the absorbing cloud discussed in D19a. The bright region in the lower part of the wind indicates that the wind is a major contributor to the very broad components of the observed emission lines.

in emission-line physics. The model predicts that lines should have a core formed in the classical BLR and strong broad wings, a profile consistent with the line deconvolution presented in Kriss et al. (2019), and that much of the UV He II and X-ray Fe K $\alpha$  can originate in the equatorial obscurer. Finally, we found that the obscurer has a modest optical depth to electron scattering and so adds reflection and scattering to the physics of the line-continuum transfer function and emission-line profiles. This is a unified model of the disk wind in which the remarkable responses of the emission lines in NGC 5548 are explained and the properties of the unobservable part of the wind are derived.

Figure 5 shows a cartoon of our derived geometry. This figure is consistent with Figure 1 of D19b, however, here we also consider the emission from the wind. The very bright area, the base of the wind, indicates this emission from the equatorial obscurer. Variations in this part of the wind produce the emission-line holiday (D19b).

This model is also consistent with the Sim et al. (2010) Monte Carlo radiative transfer predictions of the X-ray spectra of a line-driven AGN disk wind. They argued that a disk wind can easily produce a significant strong, broad Fe K $\alpha$  component which has a complex line profile. Based on their simulations, the wind’s effects on reflecting or reprocessing radiation is at least as important as the wind’s effects on the absorption signatures. Their model was later followed by Tatum et al. (2012), in which a Compton-thick disk wind is

responsible for all moderately broad Fe K emission components observed in a sample of AGNs. Their disk wind is not located in the LOS to the source and still affects the observed X-ray spectrum.

The electron scattering optical depth could be larger than estimated here,  $\tau_e \sim 0.1$ . Our derived parameters are highly approximate suggestions of the properties of the equatorial obscurer. We choose the smallest Lyman continuum optical depth (and H $^0$  column density) obscurer that is consistent with D19b. Other solutions with similar atomic column density but greater thickness are possible. They would have larger ionized column density and electron scattering optical depth. The Thomson optical depths reported in Figure 3 are normal to the slab. A ray passing into the slab at an angle  $\theta$  will see an optical depth of  $\tau_0/\cos \theta$ . For isotropic illumination the mean optical depth is  $\sqrt{2}$  larger than the normal.

A region with a significant electron scattering optical depth and warm temperature,  $T \approx 5 \times 10^4$  K, would solve several outstanding problems, which we summarize next.

It could be a part of the Compton reflector and so constitutes a translucent mirror in the inner regions. Scattering off warm gas will help producing smooth line profiles (Arav et al. 1998), a long-standing mystery in the geometry of the BLR. Gas with these properties also produces bremsstrahlung emission with a temperature similar to that deduced by Antonucci & Barvainis (1988) and so could provide the location of the non-disk emission. The obscurer modeled here is not a significant source of bremsstrahlung emission, however.

A model with an electron scattering optical depth  $\geq 0.5$  could provide an obscuration required for explaining the velocity-delay maps of Horne et al. (2020). They show that the emission from the far side of the BLR is much fainter than expected with isotropic emission from the central source and no obscuration. If the base of the wind is transparent we will observe both the near and far sides of the BLR. This indicates that there must be an obscuring cloud between the BLR and the source, acting like a mirror.

D19b proposed that the disk wind can be transparent or translucent. This hypothesis is compatible with Figure 4 of Giustini & Proga (2019), in which NGC 5548 is on the border of having a line-driven disk wind or a failed wind. This means that small changes in the disk luminosity/mass-loss rate will affect the state of the wind. The reason is that decreasing the disk luminosity leads to a reduction in the mass flux density of the wind, making it over-ionized (Proga & Kallman 2004). A transparent wind has little effect on the SED and no spectral holidays occur, while holidays occur when the wind is translucent. In this state, the equatorial obscurer absorbs a great deal of the XUV/X-ray part of the SED which must be reemitted in other spectral regions.

In this paper, we introduced a new approach to derive the wind’s properties. This will have important implications for future studies of AGN outflows and feedback. We used observations to discover the behavior of a part of the wind the can never be directly observed. Our models of the wind will be expanded to better approximate the hydrodynamics of the wind. Deriving these “next generation” hydrodynamical/microphysical models and comparing them with the observations will be the subject of our future study.

Support for HST program number GO-13330 was provided by NASA through a grant from the Space Telescope Science

Institute, which is operated by the Association of Universities for Research in Astronomy, Inc., under NASA contract NAS5-26555. We thank NSF (1816537, 1910687), NASA (17-ATP17-0141, 19-ATP19-0188), and STScI (HST-AR-15018, HST-AR-14556). M.C. acknowledges support from NASA through STScI grant HST-AR-14556.001-A and NASA grant 19-ATP19-0188, and also support from National Science Foundation through grant AST-1910687. M.D. and G.F. and F.G. acknowledge support from the NSF (AST-1816537), NASA (ATP 17-0141), and STScI (HST-AR-13914, HST-AR-15018), and the Huffaker Scholarship. M.M. is supported by the Netherlands Organization for Scientific Research (NWO) through the Innovational Research Incentives Scheme Vidi grant 639.042.525. J.M.G. gratefully acknowledges support from NASA under the ADAP award 80NSSC17K0126. M.V. gratefully acknowledges support from the Independent Research Fund Denmark via grant number DFF 8021-00130.

### ORCID iDs

M. Dehghanian <https://orcid.org/0000-0002-0964-7500>  
 G. J. Ferland <https://orcid.org/0000-0003-4503-6333>  
 G. A. Kriss <https://orcid.org/0000-0002-2180-8266>  
 B. M. Peterson <https://orcid.org/0000-0001-6481-5397>  
 K. T. Korista <https://orcid.org/0000-0003-0944-1008>  
 M. R. Goad <https://orcid.org/0000-0002-2908-7360>  
 M. Chatzikos <https://orcid.org/0000-0002-8823-0606>  
 F. Guzmán <https://orcid.org/0000-0002-2915-3612>  
 G. De Rosa <https://orcid.org/0000-0003-3242-7052>  
 M. Mehdipour <https://orcid.org/0000-0002-4992-4664>  
 J. Kaastra <https://orcid.org/0000-0001-5540-2822>  
 M. Vestergaard <https://orcid.org/0000-0001-9191-9837>  
 D. Proga <https://orcid.org/0000-0002-6336-5125>  
 M. C. Bentz <https://orcid.org/0000-0002-2816-5398>  
 S. Bisogni <https://orcid.org/0000-0003-3746-4565>

W. N. Brandt <https://orcid.org/0000-0002-0167-2453>  
 E. Dalla Bontà <https://orcid.org/0000-0001-9931-8681>  
 M. M. Fausnaugh <https://orcid.org/0000-0002-9113-7162>  
 J. M. Gelbord <https://orcid.org/0000-0001-9092-8619>  
 Keith Horne <https://orcid.org/0000-0003-1728-0304>  
 R. W. Pogge <https://orcid.org/0000-0003-1435-3053>

### References

- Antonucci, R., & Barvainis, R. 1988, *ApJL*, **332**, L13  
 Arav, N., Barlow, T. A., Laor, A., et al. 1998, *MNRAS*, **297**, 990  
 Bentz, M. C., & Katz, S. 2015, *PASP*, **127**, 67  
 Blandford, R. D., & McKee, C. F. 1982, *ApJ*, **255**, 419  
 Cappi, M., De Marco, B., Ponti, G., et al. 2016, *A&A*, **592**, A27  
 Dehghanian, M., Ferland, G. J., Kriss, G. A., et al. 2019a, *ApJ*, **877**, 119  
 Dehghanian, M., Ferland, G. J., Peterson, B. M., et al. 2019b, *ApJL*, **882**, L30  
 De Rosa, G., Peterson, B. M., Ely, J., et al. 2015, *ApJ*, **806**, 128  
 Edelson, R., Gelbord, J. M., Horne, K., et al. 2015, *ApJ*, **806**, 129  
 Fausnaugh, M. M., Denney, K. D., Barth, A. J., et al. 2016, *ApJ*, **821**, 56  
 Ferland, G. J., Chatzikos, M., Guzmán, F., et al. 2017, *RMxAA*, **53**, 385  
 Giustini, M., & Proga, D. 2019, *A&A*, **630A**, 94  
 Goad, M. R., Korista, K. T., De Rosa, G., et al. 2016, *ApJ*, **824**, 11  
 Horne, K., De Rosa, G., Peterson, B. M., et al. 2020, *ApJ*, submitted (arXiv:2003.01448)  
 Horne, K., Peterson, B. M., Collier, S. J., et al. 2004, *PASP*, **116**, 465  
 Kaastra, J. S., Kriss, G. A., Cappi, M., et al. 2014, *Sci*, **345**, 64  
 Korista, K., Baldwin, J., Ferland, G., et al. 1997, *ApJS*, **108**, 401  
 Korista, K. T., & Goad, M. R. 2000, *ApJ*, **536**, 284  
 Kriss, G. A., De Rosa, G., Ely, J., et al. 2019, *ApJ*, **881**, 153  
 Mathur, S., Gupta, A., Page, K., et al. 2017, *ApJ*, **846**, 55  
 Mehdipour, M., Kaastra, J. S., Kriss, G. A., et al. 2015, *A&A*, **575**, A22  
 Mehdipour, M., Kaastra, J. S., Kriss, G. A., et al. 2016, *A&A*, **588**, A139  
 Pei, L., Fausnaugh, M. M., Barth, A. J., et al. 2017, *ApJ*, **837**, 131  
 Peterson, B. M. 1993, *PASP*, **105**, 247  
 Peterson, B. M., Ferrarese, L., Gilbert, K. M., et al. 2004, *ApJ*, **613**, 682  
 PROGA, D., & Kallman, T. R. 2004, *ApJ*, **616**, 688  
 Sim, S. A., Proga, D., Miller, L., Long, K. S., & Turner, T. J. 2010, *MNRAS*, **408**, 1396  
 Starkey, D., Horne, K., Fausnaugh, M. M., et al. 2017, *ApJ*, **835**, 65  
 Tatum, M. M., Turner, T. J., Sim, S. A., et al. 2012, *ApJ*, **752**, 94